A&A 663, A181 (2022)
https://doi.org/10.1051/0004-6361/202142699

Astronomy & Astrophysics

Precursors of fatty alcohols in the ISM: Discovery of *n*-propanol

Izaskun Jiménez-Serra[1], Lucas F. Rodríguez-Almeida[1], Jesús Martín-Pintado[1], Víctor M. Rivilla[1,2], Mattia Melosso[3], Shaoshan Zeng[4], Laura Colzi[1,2], Yoshiyuki Kawashima[5], Eizi Hirota[6], Cristina Puzzarini[3], Belén Tercero[7], Pablo de Vicente[7], Fernando Rico-Villas[1], Miguel A. Requena-Torres[8,9], and Sergio Martín[10,11]

[1] Centro de Astrobiología (CSIC/INTA), Ctra. de Torrejón a Ajalvir km 4, 28806, Torrejón de Ardoz, Spain
e-mail: ijimenez@cab.inta-csic.es
[2] INAF – Osservatorio Astrofisico di Arcetri, Largo Enrico Fermi 5, 50125 Florence, Italy
[3] Dipartimento di Chimica "Giacomo Ciamician", Universitá di Bologna, via F. Selmi 2, 40126 Bologna, Italy
[4] Star and Planet Formation Laboratory, Cluster for Pioneering Research, RIKEN,2-1 Hirosawa, Wako, Saitama, 351-0198, Japan
[5] Department of Applied Chemistry, Faculty of Engineering, Kanagawa Institute of Technology, Atsugi, Kanagawa 240-0292, Japan
[6] The Graduate University for Advanced Studies, Hayama, Kanagawa 240-0193, Japan
[7] Observatorio de Yebes (IGN), Cerro de la Palera s/n, 19141, Guadalajara, Spain
[8] University of Maryland, College Park, ND 20742-2421, USA
[9] Department of Physics, Astronomy and Geosciences, Towson University, MD 21252, USA
[10] European Southern Observatory, Alonso de Córdova 3107, Vitacura 763 0355, Santiago, Chile
[11] Joint ALMA Observatory, Alonso de Córdova 3107, Vitacura 763 0355, Santiago, Chile

Received 19 November 2021 / Accepted 18 April 2022

ABSTRACT

Context. Theories of the origins of life propose that early cell membranes were synthesised from amphiphilic molecules simpler than phospholipids, such as fatty alcohols. The discovery in the interstellar medium (ISM) of ethanolamine, the simplest phospholipid head group, raises the question whether simple amphiphilic molecules are also synthesised in space.
Aims. We investigate whether precursors of fatty alcohols are present in the ISM.
Methods. To do this, we have carried out a spectral survey at 7, 3, 2 and 1 mm towards the Giant Molecular Cloud G+0.693-0.027 located in the Galactic centre using the IRAM 30 m and Yebes 40 m telescopes.
Results. Here, we report the detection in the ISM of the primary alcohol *n*-propanol (in both conformers *Ga*-*n*-C_3H_7OH and *Aa*-*n*-C_3H_7OH), a precursor of fatty alcohols. The derived column densities of *n*-propanol are $(5.5 \pm 0.4) \times 10^{13}$ cm^{-2} for the *Ga* conformer and $(3.4 \pm 0.3) \times 10^{13}$ cm^{-2} for the *Aa* conformer, which imply molecular abundances of $(4.1 \pm 0.3) \times 10^{-10}$ for *Ga*–*n*-C_3H_7OH and of $(2.5 \pm 0.2) \times 10^{-10}$ for *Aa*-*n*-C_3H_7OH. We also searched for the *AGa* conformer of *n*-butanol [*AGa*-*n*-C_4H_9OH] without success, yielding an upper limit to its abundance of $\leq 4.1 \times 10^{-11}$. The inferred CH_3OH:C_2H_5OH:C_3H_7OH:C_4H_9OH abundance ratios are 1:0.04:0.006:≤0.0004 towards G+0.693-0.027, that is, they decrease roughly by one order of magnitude for increasing complexity. We also report the detection of both syn and anti conformers of vinyl alcohol, with column densities of $(1.11 \pm 0.08) \times 10^{14}$ cm^{-2} and $(1.3 \pm 0.4) \times 10^{13}$ cm^{-2}, and abundances of $(8.2 \pm 0.6) \times 10^{-10}$ and $(9.6 \pm 3.0) \times 10^{-11}$, respectively.
Conclusions. The detection of *n*-propanol, together with the recent discovery of ethanolamine in the ISM, opens the possibility that precursors of lipids according to theories of the origin of life, could have been brought to Earth from outer space.

Key words. ISM: molecules – ISM: clouds – Galaxy: center – astrochemistry – line: identification

1. Introduction

Compartmentalisation (i.e. the formation of vesicles or small membranes) is an essential step in the emergence of life. Theories of the origin of life such as prebiotic systems chemistry (Ruiz-Mirazo et al. 2014) propose that compartmentalisation had to appear concurrently with the first metabolic and replicative systems forming proto-cells. It is thought that the composition of primordial membranes was much simpler than that of modern cells. Several families of amphiphilic molecules such as alkyl phosphates, alkyl sulphates, fatty acids, and fatty alcohols have been proposed as possible prebiotic lipids, that is, as constituents of proto-membranes (Ruiz-Mirazo et al. 2014). Among them, fatty alcohols (also called primary alcohols) present a simple structure consisting of a straight chain with the OH group linked to a primary carbon (i.e. forming a -CH_2OH group).

Two possible scenarios have been proposed for the formation of prebiotic lipids: they could form endogenously under early Earth conditions for instance via Fischer-Tropsch synthesis (Nooner et al. 1976; McCollom et al. 1999; Ruiz-Mirazo et al. 2014), or they could be synthesised exogenously in interstellar space and incorporated to Solar System materials such as interplanetary dust particles, comets, and meteorites (Bernstein et al. 1999). Although not all examined meteorites contain long-chain amphiphiles (Deamer et al. 1994), Deamer (1985) showed that the amphiphilic compounds found in the Murchison meteorite can form vesicle-like structures under certain prebiotic conditions. Using the different contributions to organic matter delivery analysed by Chyba & Sagan (1992, see their Table 2), Ruiz-Mirazo et al. (2014) estimated that a total amount of $\sim 10^{16}$–10^{18} kg of extraterrestrial organic matter was delivered to Earth during the Late Heavy Bombardment period

(mainly between 3.9 and 3.8 billion years ago), which supports the idea that extraterrestrial material could have contributed to the emergence of prebiotic lipids in an early Earth[1].

The recent discovery of ethanolamine ($NH_2CH_2CH_2OH$), the simplest head group of phospholipids (Rivilla et al. 2021a), in the interstellar medium (ISM), has raised the interest for the search of precursors of prebiotic lipids in space, and in particular, of other alcohols. For fatty alcohols, the only ones that have been observed in the ISM are methanol (CH_3OH) and ethanol (C_2H_5OH), which are practically ubiquitous in the ISM (see e.g. Jorgensen et al. 2020; Martín et al. 2021, and references therein). *n*-propanol (also named 1-propanol; molecular formula $CH_3CH_2CH_2OH$ or C_3H_7OH) has been searched for in the ISM, but no detection has been reported to date (Tercero et al. 2015; Müller et al. 2016; Qasim et al. 2019a; Manigand et al. 2021). However, primary alcohols, including propanol, have been detected in comet 67P/Churyumov-Gerasimenko (Altwegg et al. 2019), which suggests that this molecule could be formed under interstellar conditions.

In this work, we report the discovery of *n*-propanol towards the Giant Molecular Cloud (GMC) G+0.693-0.027 (hereafter G+0.693) located in the Galactic centre. We also report the detection of both syn and anti conformers of vinyl alcohol (CH_2CHOH) towards the same cloud. The syn conformer was tentatively detected towards SgrB2(N) by Turner & Aponi (2001), but this detection was never confirmed in higher-sensitivity observations carried out with ALMA (Martin-Drumel et al. 2019). More recently, Agúndez et al. (2021) have unambiguously identified the syn conformer towards TMC-1. However, to our knowledge, this is the first time that the anti conformer of this molecule is robustly detected in the ISM.

G+0.693 is known to be one of the most chemically rich interstellar sources in our Galaxy (Requena-Torres et al. 2006, 2008; Zeng et al. 2018), despite the fact it does not show any sign of high-mass star formation activity (Zeng et al. 2020). The chemistry of this cloud is characterised by the presence of low-velocity shocks (its emission shows broad line widths of $\sim$20 km s^{-1} and high abundances of HNCO, a typical molecular tracer of low-velocity shocks; Martín et al. 2008), which sputter the molecular content of the icy mantles of dust grains into the gas phase (see e.g. Jiménez-Serra et al. 2008). The H_2 gas densities in G+0.693 are of the order of a few 10^4 cm^{-3} (Zeng et al. 2020), and the gas kinetic temperatures range from 70 to 150 K, as measured using CH_3CN (Zeng et al. 2018). Due to the low H_2 gas densities, the molecular line emission from high dipole moment molecules such as complex organics is subthermally excited, and their excitation temperature lies below 20 K (Requena-Torres et al. 2006; Zeng et al. 2018). This represents an advantage for the search of new molecular species since the millimetre spectra observed towards this source present rather low levels of line blending and line confusion. As a result, G+0.693 has yielded several first detections of new molecular species in the ISM, including *Z*-cyanomethanimine (Z-HNCHCN; Rivilla et al. 2019), hydroxylamine (NH_2OH; Rivilla et al. 2020), ethanolamine ($NH_2CH_2CH_2OH$; Rivilla et al. 2021a), the cyanomydil radical (HNCN; Rivilla et al. 2021b), mono-thioformic acid (HC(O)SH; Rodríguez-Almeida et al. 2021a), ethyl isocyanate (C_2H_5NCO; Rodríguez-Almeida et al. 2021b), and PO^+ (Rivilla et al. 2022). Urea, an important prebiotic molecule (Becker et al. 2019; Belloche et al. 2019), has also been detected towards this cloud (Jiménez-Serra et al. 2020).

[1] Note that the total amount of organic matter in the present biosphere is about 6×10^{14} kg (Bar-On et al. 2018).

The paper is organised as follows. In Sect. 2 we describe the observations, and in Sect. 3 we present the detections of *n*-propanol and the syn and anti forms of vinyl alcohol. We also report the upper limits to the non-detections of isopropanol (i-C_3H_7OH), ethyl methyl ether ($CH_3OCH_2CH_3$), cyclopropanol (c-C_3H_5OH), and *n*-butanol (n-C_4H_9OH). In Sect. 4 we discuss the chemistry of *n*-propanol and vinyl alcohol and place these detections in context with previous works and with theories of the origin of life. Finally, in Sect. 5 we present our conclusions.

2. Observations

We have carried out a spectral line survey at 1, 2, 3, and 7 mm toward G+0.693 with the Instituto de Radioastronomía Milimétrica (IRAM) 30 m telescope (Granada, Spain) and the Yebes 40 m telescope (Guadalajara, Spain). The spectral coverage extends from 32 to 233 GHz, and the data were smoothed to a typical velocity resolution of $\sim$1.5–2.5 km s^{-1}. The equatorial coordinates of the source are α(J2000) = 17^{h}47^{m}22^s and δ(J2000) = −28°21′27″. We used the position-switching mode with an off position located at (−885″, 290″) with respect to G+0.693. Each frequency setup was repeated by shifting the central frequency by 20–100 MHz in order to identify spurious lines or contamination from the image band.

The IRAM 30 m observations were performed during three sessions in 2019: 10–16 April, 13–19 August, and 11–15 December. The EMIR E090, E150, and E230 receivers were used together with the fast Fourier transform spectrometers (FFTS) with a frequency resolution of 200 kHz (equivalent to a velocity resolution between 0.8 and 0.26 km s^{-1} at 3 and 1 mm, respectively). The IRAM 30 m beam size ranged from $\sim$34″ to 11″ when going from 72 to 233 GHz. The observations with the Yebes 40 m radiotelescope were carried out between the 3–9 and 15–22 February 2020. The Nanocosmos *Q*-band (7 mm) HEMT receiver was used, which enabled ultra broad-band observations with an instantaneous bandwidth of 18.5 GHz per polarisation between 31.3 and 50.6 GHz (Tercero et al. 2021). The 16 FFTS provided a channel width of 38 kHz, which corresponds to a velocity resolution of 0.22–0.36 km s^{-1}. The Yebes 40 m beam size ranged from $\sim$54″ to 36″ when moving from 31 to 50 GHz. The line intensity of all spectra was measured in units of T_A^* as the molecular emission toward G+0.693 is extended compared to the main beam of the telescopes (Requena-Torres et al. 2006; Zeng et al. 2020).

3. Analysis and results

3.1. Detection of the Ga and Aa conformers of n-propanol

We used the data analysis package MADCUBA[2] (Martín et al. 2019) to search for all transitions from the *Ga*, *Aa*, *Gg*, and *Gg′* conformers of *n*-propanol (or 1-propanol) within our dataset (see Fig. 1). We were unable to search for the *Ag* conformer because its energy levels are heavily perturbed by the *Aa* species and the spectroscopic parameters have not been reported so far (see Kisiel et al. 2010). The relative energies of the *n*-propanol conformers are E = 0 K for *Ga*, E = 40.3 K for *Aa*, E = 64.7 K for *Ag*, E = 68.8 K for *Gg*, and E = 73.2 K for *Gg′* (Kisiel et al. 2010). We note, however, that the conformers of *n*-propanol were modelled

[2] MADCUBA, or MAdrid Data CUBe Analysis, is a software developed at the Center of Astrobiology in Madrid: https://cab.inta-csic.es/madcuba/index.html

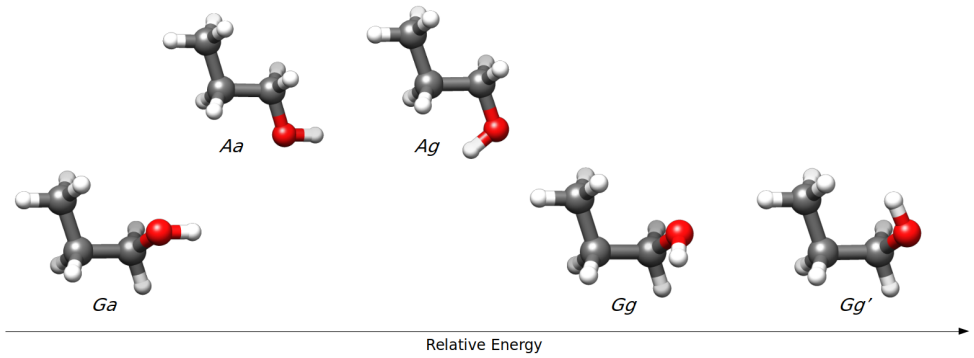

Fig. 1. Conformers of *n*-propanol (*n*-C_3H_7OH) represented as a function of relative energy. The two lowest-energy conformers are the *Ga* and *Aa* conformers, which have been detected towards G+0.693 (see Sect. 3.1). The *x*-axis is not to scale for visualisation purposes. The relative energies of the different conformers of *n*-propanol are E = 0 K for *Ga*, E = 40.3 K for *Aa*, E = 64.7 K for *Ag*, E = 68.8 K for *Gg*, and E = 73.2 K for *Gg′* (see also Sect. 3.1).

independently (i.e. without taking their zero-point energy into account) as it has been done in the past for other species towards G+0.693 such as imines, for which both the low- and high-energy conformers have been detected (see Rivilla et al. 2019). Our data reveal that only the two lowest-energy conformers, *Ga* and *Aa* (hereafter *Ga*-*n*-C_3H_7OH and *Aa*-*n*-C_3H_7OH, respectively; see Fig. 1), are detected towards G+0.693 (see below). The spectroscopic information of *Ga*-*n*-C_3H_7OH was extracted from the Cologne Database for Molecular Spectroscopy catalog (CDMS, entry 060505; Endres et al. 2016), which was derived from the rotational spectrum measured by Kisiel et al. (2010). The spectroscopic information for the remaining conformers of *n*-propanol was obtained by us using the data from Dreizler & Scappini (1981) and Kisiel et al. (2010).

The line identification and analysis of the transitions of *Ga*-*n*-C_3H_7OH and *Aa*-*n*-C_3H_7OH was carried out using the tool called spectral line identification and modelling (SLIM) of MADCUBA. SLIM uses the spectroscopic data entries from the molecular catalogues to generate synthetic spectra under the assumption of local thermodynamic equilibrium (LTE) and by considering line opacity effects. The LTE fit that best matches the observed line spectra of *Ga*-*n*-C_3H_7OH and *Aa*-*n*-C_3H_7OH provides the derived values for the molecular column densities (N), excitation temperatures (T_{ex}), central radial velocities of the gas (v_{LSR}), and the full widths at half maximum (FWHM) of the line emission.

Figures 2 and 3 present the unblended and slightly blended transitions of *Ga*-*n*-C_3H_7OH and *Aa*-*n*-C_3H_7OH, respectively, detected towards G+0.693. Table 1 reports the spectroscopic information of the transitions from these species together with the rms noise level measured in the spectra (rms), the derived integrated line intensities ($\int T_A^* \mathrm{d}v$) and the signal-to-noise ratio (S/N) (also in integrated intensity) obtained with MADCUBA-SLIM. The rms noise level (rms) was calculated at the velocity resolution reported in Table 1 using all the line-free parts of each spectrum within a velocity range of $\pm 200\,\mathrm{km\,s^{-1}}$ around each line. For the spectra with too few available line-free parts, a velocity range of $\pm 600\,\mathrm{km\,s^{-1}}$ around each line was used. To improve the visualisation of the detected lines, some of the spectra were smoothed to a velocity resolution of 4–8 $\mathrm{km\,s^{-1}}$, enough to provide ≥3 resolution elements over the line width. We stress that the smoothing of the lines does not affect our analysis in any form, as demonstrated by Rivilla et al. (2020).

In Figs. 2 and 3 and Table 1, we indicate the transitions that provide the identification of *Ga*-*n*-C_3H_7OH and *Aa*-*n*-C_3H_7OH with asterisks. All these transitions have an $S/N \geq 6$, where the error in the integrated intensity of the lines is calculated as $\mathrm{rms} \times \sqrt{\delta v \times \Delta v}$, where δv is the velocity resolution of the spectra and Δv is the FWHM of the line emission. We note, however, that if a more conservative approach were taken (i.e. if we considered Δv as the full velocity range covered by the line), then the S/N would be lower by a factor sqrt(2) = 1.4. This would not affect the identification of the species reported here because all the bright lines that contribute to the identification of *Ga*-*n*-C_3H_7OH and *Aa*-*n*-C_3H_7OH would have an $S/N \geq 4.5$ even after correcting by this factor. The remaining transitions of *Ga*-*n*-C_3H_7OH and *Aa*-*n*-C_3H_7OH reported in Table 1 and Figs. 2 and 3 without asterisks demonstrate that they are consistent with the species identification and their LTE fits. Figures 2 and 3 also show the $3 \times$ rms noise level in intensity (dotted black lines) and the $3 \times \mathrm{rms}/\sqrt{N}$ level (with N the number of channels across the FWHM), which is associated with the noise level in integrated intensity, that is, our detectability criterion (see the dotted red lines).

The $6_{6,X} \rightarrow 5_{5,X}$, $4_{4,X} \rightarrow 3_{3,X}$, and $3_{1,2} \rightarrow 2_{0,2}$ transitions of *Ga*-*n*-C_3H_7OH at 162 332, 10 5032, and 40 341 MHz, respectively (see Fig. 2), are partly blended with HSC, *s*-propanal, and C_2H_5NCO lines of similar intensity (see the detections of some of these species in Rivilla et al. 2020; Rodríguez-Almeida et al. 2021b). However, we note that the global LTE fit (i.e. considering all molecular species) of the spectra at these frequencies perfectly matches the observed spectra (see the black histograms and solid blue lines in Fig. 2). For *Aa*-*n*-C_3H_7OH (see Fig. 3), the $10_{1,10} \rightarrow 9_{0,9}$ and $9_{2,8} \rightarrow 9_{1,9}$ transitions are likely blended with lines from unidentified species, in addition to a small contribution from $(CH_2OH)_2$ for the $10_{1,10} \rightarrow 9_{0,9}$ line (see Table 1). The derived S/N of the $3_{1,3} \rightarrow 2_{0,2}$ transition should be taken with caution since the LTE fit performed by MADCUBA-SLIM overpredicts the integrated intensity of this line. The remaining *Ga*-*n*-C_3H_7OH and *Aa*-*n*-C_3H_7OH transitions that we considered in our analysis but that are not shown here are consistent with their MADCUBA-SLIM LTE fits, although they appear heavily blended with lines from other molecular species.

The best LTE fit of the *Ga*-*n*-C_3H_7OH lines is obtained for a column density of $\mathrm{N}(Ga\text{-}n\text{-}C_3H_7OH) = (5.5 \pm 0.4) \times 10^{13}\,\mathrm{cm^{-2}}$ and a $T_{ex} = 14$ K, $V_{LSR} = 65.9 \pm 1.0\,\mathrm{km\,s^{-1}}$ and $\Delta v = 20\,\mathrm{km\,s^{-1}}$ (T_{ex} and Δv needed to be fixed for the SLIM-AUTOFIT algorithm to find convergence). For *Aa*-*n*-C_3H_7OH, the best fit of the lines was reached for a $\mathrm{N}(Aa\text{-}n\text{-}C_3H_7OH) = (3.4 \pm 0.3) \times 10^{13}\,\mathrm{cm^{-2}}$ and a $T_{ex} = 12.5 \pm 2.0$ K after fixing the central radial velocity and the FWHM of the source to $V_{LSR} = 69\,\mathrm{km\,s^{-1}}$ and $\Delta v = 20\,\mathrm{km\,s^{-1}}$. The derived and assumed T_{ex}, V_{LSR} and Δv are consistent with those measured for other molecular species towards this source (see e.g. Requena-Torres et al. 2006; Zeng et al. 2018; Rivilla et al. 2020, 2021a; Rodríguez-Almeida et al. 2021a) and with the results obtained from the rotational diagrams of *Ga*-*n*-C_3H_7OH and *Aa*-*n*-C_3H_7OH shown in Figs. A.1 and A.2.

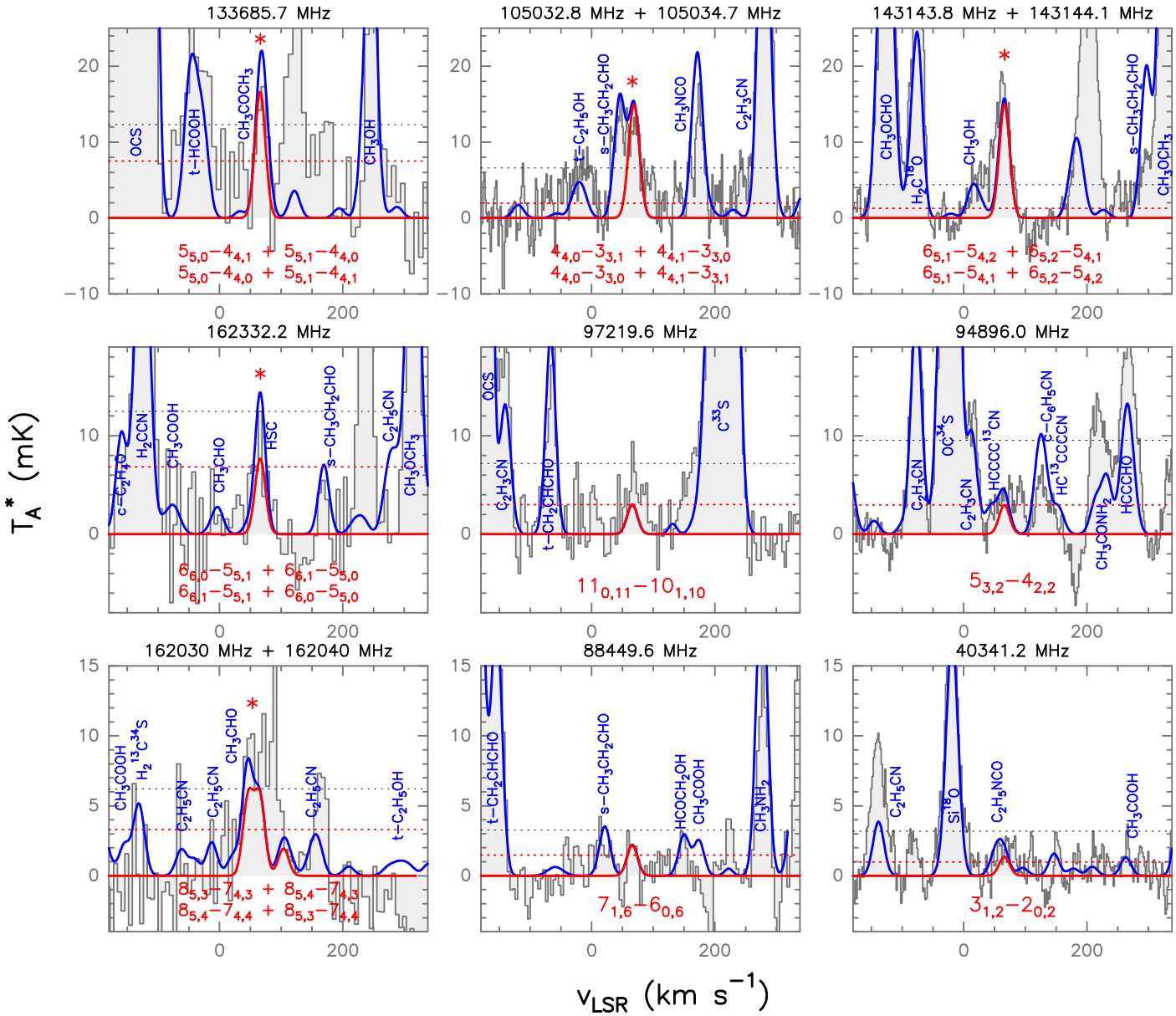

Fig. 2. Unblended and slightly blended transitions of *Ga*-*n*-C_3H_7OH detected towards G+0.693. The histogram and grey shaded area correspond to the observed IRAM 30 m and Yebes 40 m spectra. Red lines indicate the best LTE fit to the lines of *Ga*-*n*-C_3H_7OH reported in Table 1. Blue lines show the overall fit to the observed spectra considering all molecular species detected in G+0.693. The quantum numbers of the *Ga*-*n*-C_3H_7OH transitions are indicated in red at the bottom of the panels, while blue labels present the species identified in the shown spectra. The frequencies of the lines are shown in the upper part of each panel. The red asterisks indicate the transitions that provide the identification of *Ga*-*n*-C_3H_7OH. Dotted black lines indicate the $3\times$rms level in intensity in the spectra. Dotted red lines show the detectability limit in the integrated area defined as $3\times\mathrm{rms}/\sqrt{N}$, with N the number of channels across the line width.

To derive the abundances of the *Ga* and *Aa* conformers of propanol, we assumed a H_2 column density of 1.35×10^{23} cm^{-2} as measured towards G+0.693 (Martín et al. 2008). This provides an abundance of $(4.1\pm0.3)\times10^{-10}$ for *Ga*-*n*-C_3H_7OH and of $(2.5\pm0.2)\times10^{-10}$ for *Aa*-*n*-C_3H_7OH. The abundance ratio of the two detected conformers of *n*-propanol is *Ga*/*Aa* = 1.64. Considering this ratio and that the *Aa* conformer lies ~40 K above *Ga*, we can determine whether these two isomers are in thermodynamic equilibrium. With Eq. (3) of Rivilla et al. (2019), the derived T_{kin} is ~80 K, consistent with the kinetic temperature range measured from CH_3CN towards G+0.693 (between 70 and 150 K; see Zeng et al. 2018). The calculated *Ga*/*Aa* abundance ratio therefore suggests that both species are in thermodynamic equilibrium (understood as the equilibration between the abundances of the *Ga* and *Aa* conformers), as observed for other species such as the E/Z isomers of imines (see García de la Concepción et al. 2021).

The derived upper limits to the other two conformers of *n*-propanol for which spectroscopic data exist (*Gg* and *Gg*′) are presented in Table 2. They were calculated using the rms noise level of the brightest less blended transition spectra, and assuming a T_{ex} = 12.5 K, that is, the same T_{ex} as was inferred from *Aa*-*n*-C_3H_7OH (see above). The derived upper limits to their column densities and abundances are $\leq1.6\times10^{13}$ cm^{-2} and $\leq1.2\times10^{-10}$ for *Gg*-*n*-C_3H_7OH, and $\leq5.7\times10^{12}$ cm^{-2} and $\leq4.2\times10^{-11}$ for *Gg*′-*n*-C_3H_7OH (see Table 2), respectively.

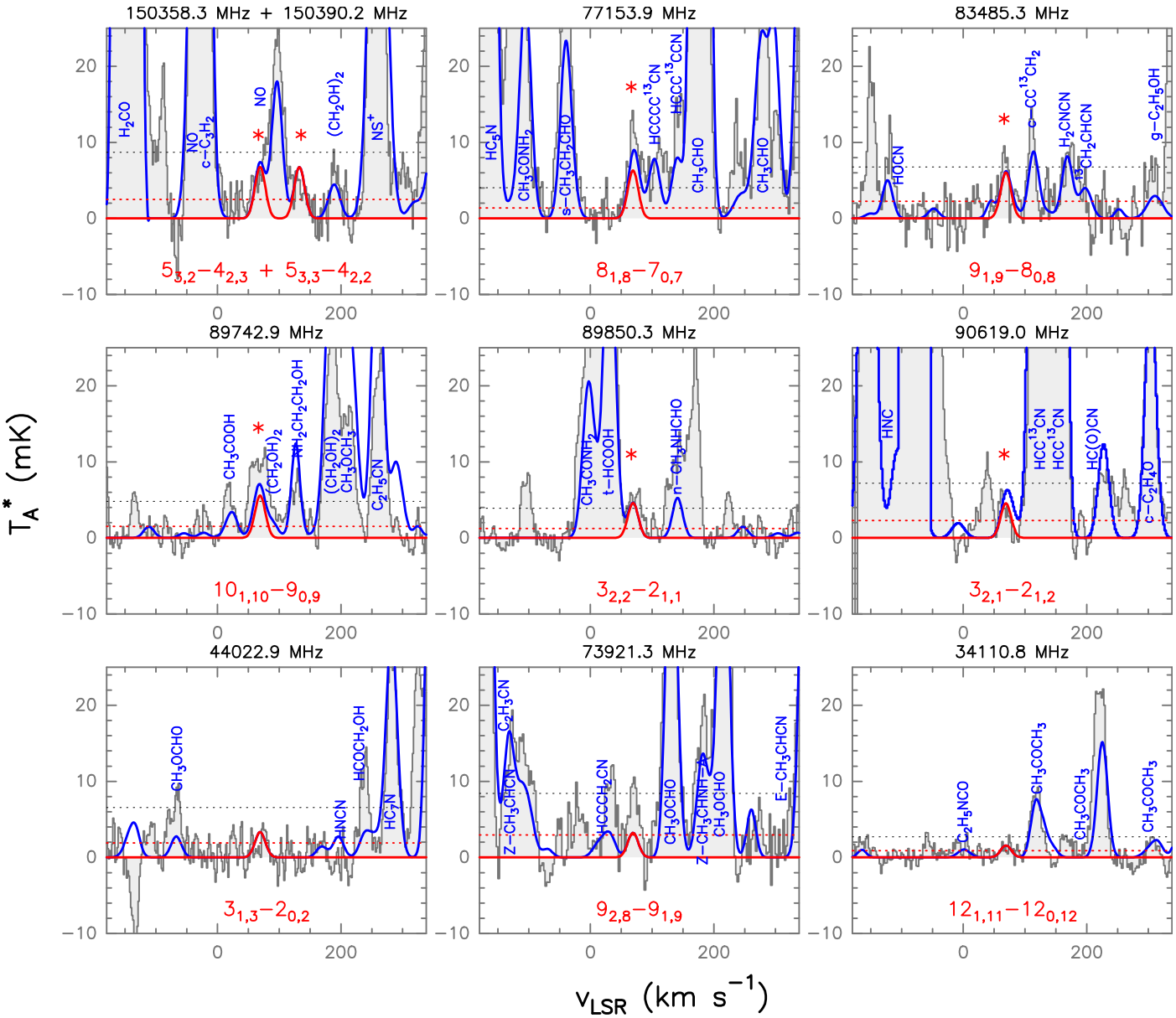

Fig. 3. Unblended and slightly blended transitions of *Aa*-*n*-C_3H_7OH detected towards G+0.693. The histogram, grey shaded area, colour lines, and labels are as in Fig. 2. Red lines indicate the best LTE fit to the lines of *Aa*-*n*-C_3H_7OH reported in Table 1. The frequencies of the lines are shown in the upper part of each panel, while the red asterisks indicate the transitions that contribute to the identification of *Aa*-*n*-C_3H_7OH. Dotted black lines indicate the $3\times$rms level in intensity in the spectra. Dotted red lines show the detectability limit in the integrated area defined as $3\times\mathrm{rms}/\sqrt{N}$, with N the number of channels across the line width.

By using the abundance ratios *Ga*/*Gg* and *Ga*/*Gg*′, we can investigate whether the *Gg* and *Gg*′ conformers are also in thermodynamic equilibrium. The derived abundance ratios *Ga*/*Gg* ≥ 3.4 and *Ga*/*Gg*′ ≥ 9.7 yield kinetic temperatures $T_{\rm kin}\leq$56 K and $T_{\rm kin}\leq$32 K, respectively. These kinetic temperatures are lower than those measured towards G+0.693 (Zeng et al. 2018), which suggests that only the lower-energy conformers of a molecular species could reach thermodynamic equilibrium via mechanisms such as multi-dimensional quantum tunnelling, as found for imines and acids (see García de la Concepción et al. 2021, 2022).

3.2. Search of isopropanol (*i*-propanol) and ethyl methyl ether

Isopropanol (also named isopropyl alcohol and 2-propanol) is a structural isomer of *n*-propanol. Its chemical formula is $CH_3CH(OH)CH_3$. We have searched for the gauche and anti conformers of *i*-propanol (*g*-*i*-C_3H_7OH and *a*-*i*-C_3H_7OH, respectively) in our dataset by using entries 060518 and 060519 of the CDMS molecular catalogue (Endres et al. 2016), obtained using the spectroscopic work of Maeda et al. (2006). The anti conformer is about 120 K higher in energy than the doubly degenerate gauche conformer.

None of the two conformers of *i*-propanol are detected (see Table 2), with upper limits to their column densities of $\leq 8.5\times10^{12}$ cm^{-2} for *g*-*i*-C_3H_7OH and $\leq 3.9\times10^{12}$ cm^{-2} for *a*-*i*-C_3H_7OH. These column densities translate into abundance upper limits of $\leq 6.3\times10^{-11}$ and $\leq 2.9\times10^{-11}$ for the gauche and anti conformers of *i*-propanol, respectively.

Propanol has a third structural isomer: ethyl methyl ether ($CH_3OCH_2CH_3$ or methoxyethane). We have also searched for the trans conformer of this species (the lowest in energy) in

Table 1. Unblended or slightly blended transitions of *Ga*-*n*-C_3H_7OH and *Aa*-*n*-C_3H_7OH detected towards G+0.693.

Frequency (MHz)	QNs $(J''_{K_a'',K_c''} - J'_{K_a',K_c'})$	E_u (K)	log I(300K) (nm^2 MHz)	rms (mK)	δv (km s^{-1})	$\int T_A^* dv$ (mK km s^{-1})	S/N [a]	Blending
				Ga-*n*-C_3H_7OH				
40 341.1539	$3_{1,2}$–$2_{0,2}$	3.3	–6.4573	1.1	1.9	28.9(6.5) [b]	4.5	Blended with C_2H_5NCO
88 449.6240	$7_{1,6}$–$6_{0,6}$	13.6	–5.6188	1.1	4.2	47.5(9.9)	4.8	Clean transition
94 895.9659	$5_{3,2}$–$4_{2,2}$	11.0	–5.5443	3.2	1.9	63.2(20.0)	3.2	Blended with HCCCC^{13}CN
97 219.5786	$11_{0,11}$–$10_{1,10}$	28.8	–5.0046	2.4	3.8	63.6(20.8)	3.1	Clean transition
105 032.7600 [*]	$4_{4,1}$–$3_{3,0}$	11.9	–5.3260	2.2	1.7	335.6(13.0) [c]	25.7 [c]	Clean transition [c,d]
105 032.8215 [*]	$4_{4,0}$–$3_{3,0}$	11.9	–5.3814	2.2	1.7	–	–	–
105 034.6719 [*]	$4_{4,1}$–$3_{3,1}$	11.9	–5.3814	2.2	1.7	–	–	–
105 034.7334 [*]	$4_{4,0}$–$3_{3,1}$	11.9	–5.3259	2.2	1.7	–	–	–
133 685.6682 [*]	$5_{5,0}$–$4_{4,1}$	18.3	–5.0148	4.1	7.3	354.9(50.0) [c]	7.1 [c]	Slightly blended with CH_3COCH_3 [c,d]
133 685.6682 [*]	$5_{5,1}$–$4_{4,0}$	18.3	–5.0148	4.1	7.3	–	–	–
133 685.6682 [*]	$5_{5,1}$–$4_{4,1}$	18.3	–5.0718	4.1	7.3	–	–	–
133 685.6682 [*]	$5_{5,0}$–$4_{4,0}$	18.3	–5.0718	4.1	7.3	–	–	–
143 143.8136 [*]	$6_{5,2}$–$5_{4,1}$	21.1	–4.9557	1.5	1.7	320.2(8.5) [c]	37.7 [c]	Clean transition [c,d]
143143.8332 [*]	$6_{5,1}$–$5_{4,1}$	21.1	–5.0037	1.5	1.7	–	–	–
143 144.1096 [*]	$6_{5,1}$–$5_{4,2}$	21.1	–4.9557	1.5	1.7	–	–	–
143 144.1096 [*]	$6_{5,2}$–$5_{4,2}$	21.1	–5.0037	1.5	1.7	–	–	–
162 029.4986 [*]	$8_{5,4}$–$7_{4,3}$	27.9	–4.8415	2.1	6.0	238.8(22.7) [c]	10.5 [c]	Slightly blended with CH_3CHO [c,d]
162 030.2797 [*]	$8_{5,3}$–$7_{4,3}$	27.9	–4.8688	2.1	6.0	–	–	–
162 039.5868 [*]	$8_{5,4}$–$7_{4,4}$	27.9	–4.8687	2.1	6.0	–	–	–
162 040.3663 [*]	$8_{5,3}$–$7_{4,4}$	27.9	–4.8415	2.1	6.0	–	–	–
162 332.1928 [*]	$6_{6,0}$–$5_{5,1}$	26.1	–4.7688	4.2	6.0	307.0(46.0) [c]	6.7 [c]	Slightly blended with HSC [c]
162 332.1928 [*]	$6_{6,1}$–$5_{5,0}$	26.1	–4.7688	4.2	6.0	–	–	–
162 332.1928 [*]	$6_{6,1}$–$5_{5,1}$	26.1	–4.8267	4.2	6.0	–	–	–
162 332.1928 [*]	$6_{6,0}$–$5_{5,0}$	26.1	–4.8267	4.2	6.0	–	–	–
				Aa-*n*-C_3H_7OH				
34 110.7596	$12_{1,11}$-$12_{0,12}$	29.1	–5.4467	0.9	2.2	33.6(6.0) [b]	5.6	Clean transition
44022.8732	$3_{1,3}$-$2_{0,2}$	3.2	–5.8803	2.2	1.7	71.0(12.8)	5.5 [e]	Clean transition
73 921.2560	$9_{2,8}$-$9_{1,9}$	20.2	–5.1140	2.8	2.5	69.2(20.0)	3.5	Blended with U species
77 153.9362 [*]	$8_{1,8}$-$7_{0,7}$	13.6	–5.0315	1.4	2.4	134.2(9.3)	14.4	Slightly blended with n-C_3H_7CN [d]
83 485.2943 [*]	$9_{1,9}$-$8_{0,8}$	16.7	–4.9139	2.3	2.2	128.9(15.0)	8.6	Clean transition [d]
89 742.8720 [*]	$10_{1,10}$-$9_{0,9}$	20.2	–4.8060	1.6	2.0	118.6(10.3)	11.5	Slightly blended with $(CH_2OH)_2$ and U-line [d]
89 850.2691 [*]	$3_{2,2}$-$2_{1,1}$	6.5	–5.3442	1.3	2.0	98.0(8.3)	11.8	Clean transition [d]
90 618.9845 [*]	$3_{2,1}$-$2_{1,2}$	6.5	–5.3441	2.4	2.0	97.3(15.3)	6.4	Slightly blended with HCC^{13}CN
150 358.3345 [*]	$5_{3,3}$-$4_{2,2}$	15.1	–4.6853	2.9	1.6	144.2(16.6)	8.7	Clean transition
150 390.2490 [*]	$5_{3,2}$–$4_{2,3}$	15.1	–4.6852	2.9	1.6	144.2(16.6)	8.7	Clean transition

Notes. [a]The S/Ns are calculated from the integrated intensity of the lines inferred from the LTE fits of MADCUBA-SLIM. They are not calculated from the Gaussian fits of individual lines. [b]The error in the integrated intensity is calculated as rms $\times \sqrt{\delta v \times \Delta v}$, with δv the velocity resolution of the spectra and Δv the FWHM of the line emission of 20 km s^{-1}. [c]The line corresponds to a blend of four individual *Ga*-*n*-C_3H_7OH transitions. The total integrated intensity and the S/N are calculated from the sum of the areas of the individual transitions. [d]Transitions detected at the ≥3 rms noise level in peak intensity. [e]This S/N should be taken with caution since the LTE fit carried out by MADCUBA-SLIM overpredicts the integrated intensity of the line. [*]Transitions that provide the identification of the species with S/N ≥ 6 in integrated intensity.

our dataset by using the spectroscopic information reported by Fuchs et al. (2003) and by inserting the entry for this species in CDMS/JPL format into MADCUBA. This species has not been detected towards G+0.693 either, with upper limits to its column density and abundance of $\leq 3.8 \times 10^{13}$ cm^{-2} and $\leq 2.8 \times 10^{-10}$ (see Table 2), respectively.

3.3. Other alcohols: detection of the syn and anti forms of vinyl alcohol

We have also searched for other alcohols within our spectroscopic survey towards G+0.693. We targeted vinyl alcohol (or ethenol, with formula H_2C=CHOH), cyclopropanol (c-C_3H_5OH) and *n*-butanol (*n*-C_4H_9OH). We used the CDMS entries 044506 and 044507 for the syn and anti forms of vinyl alcohol (*s*-H_2C=CHOH and *a*-H_2C=CHOH in CDMS; Endres et al. 2016) based on the spectroscopic work of Melosso et al. (2019). The syn form of vinyl alcohol is the lowest in energy, with the anti form lying about 4.6 kJ mol^{-1} (or 550 K) above the syn form (Rodler 1985). For cyclopropanol (c-C_3H_5OH), we took the spectroscopic information for the gauche conformer (the most stable one) from the work of Macdonald et al. (1978) and inserted the entry for this species in CDMS/JPL format into MADCUBA. In the same way, for *n*-butanol (both *AGa*-(E) and *AGa*-(A) methyl internal rotation substates), we calculated their spectroscopic information from the laboratory experiments and theoretical calculations of Kawashima et al. (2021).

Table 2. Upper limits obtained for the *Gg* and *Gg′* conformers of *n*-propanol for the anti and gauche conformers of i-propanol, and for the trans conformer of ethyl methyl ether.

Species	Formula	Frequency (MHz)	QNs ($J''_{K''_a,K''_c}$ - $J'_{K'_a,K'_c}$)	E_u (K)	log I(300 K) (nm^2 MHz)	rms (mK)	N [(a)] (cm^{-2})	Abundance [(b)]
n-propanol (*Gg*)	*Gg*-*n*-C_3H_7OH	75 699.1096	$3_{3,1}-2_{2,1}$	75.7	–6.1471	2.3	$\leq 1.6\times10^{13}$ [(c)]	$\leq 1.2\times10^{-10}$
		75 700.5781	$3_{3,0}-2_{2,1}$	75.7	–6.2273	2.3	–	–
n-propanol (*Gg′*)	*Gg′*-*n*-C_3H_7OH	87 730.9823	$10_{1,10}-9_{1,9}$	97.0	–5.2641	0.9	$\leq 5.7\times10^{12}$	$\leq 4.2\times10^{-11}$
Isopropanol (gauche)	*g*-*i*-C_3H_7OH	88 532.3081	$4_{1,4}-3_{1,3}$	7.5	–5.7726	1.8	$\leq 8.5\times10^{12}$ [(c)]	$\leq 6.3\times10^{-11}$
		88 538.5001	$4_{0,4}-3_{0,3}$	7.5	–5.7737	1.8	–	–
Isopropanol (anti)	*a*-*i*-C_3H_7OH	79 734.1627	$8_{1,8}-7_{0,7}$	137.9	–5.5140	2.7	$\leq 3.9\times10^{12}$ [(c)]	$\leq 2.9\times10^{-11}$
		79 734.1627	$8_{0,8}-7_{1,7}$	137.9	–5.5140	2.7	–	–
Ethyl methyl ether (trans)	*t*-$CH_3OCH_2CH_3$	73 243.2848	$4_{2,3}-4_{1,4}$	8.5	–5.6357	2.7	$\leq 3.8\times10^{13}$	$\leq 2.8\times10^{-10}$

Notes. [(a)]Upper limits to the column densities calculated assuming a T_{ex}=12.5 K, i.e. the same as the one derived for *Aa*-*n*-C_3H_7OH, and after fixing V_{LSR} = 69 km s^{-1} and Δv = 20 km s^{-1} (see Sect. 3.1). [(b)]Abundances were derived considering a H_2 column density of 1.35×10^{23} cm^{-2} (Martín et al. 2008). [(c)]Upper limits were obtained considering the two transitions shown in the table, which appear blended in the spectra. The selected transitions are the cleanest and the brightest of all the lines covered in our observations.

Table 3. Selected lines of the two forms of vinyl alcohol (H_2C=CHOH), syn *(s)* and anti *(a)* detected towards G+0.693.

Frequency (MHz)	QNs ($J''_{K''_a,K''_c}$ - $J'_{K'_a,K'_c}$)	E_u (K)	log I(300K) (nm^2 MHz)	rms (mK)	δv (km s^{-1})	$\int T_A^* dv$ (K km s^{-1})	S/N [(a)]	Blending
				s-H_2C=CHOH				
37 459.19 [(*)]	$2_{1,2}-1_{1,1}$	5.09	–6.3478	1.1	2.0	0.103(0.007) [(c)]	14.7	Clean transition [(b)]
39 016.31 [(*)]	$2_{0,2}-1_{0,1}$	2.81	–6.1842	1.2	1.9	0.193(0.007)	25.9	Clean transition [(b)]
40 650.65 [(*)]	$2_{1,1}-1_{1,0}$	5.32	–6.2770	1.3	1.9	0.109(0.008)	13.8	Clean transition [(b)]
74 842.40 [(*)]	$4_{1,4}-3_{1,3}$	11.38	–5.3566	3.2	2.4	0.244(0.022)	10.9	Slightly blended with t-HCOOH and HCCHO [(b)]
86 557.56 [(*)]	$2_{1,2}-1_{0,1}$	5.09	–5.3840	2.4	2.1	0.454(0.016)	29.1	Slightly blended with t-HCOOH and c-HCOOH [(b)]
142 348.06 [(*)]	$4_{2,2}-4_{1,3}$	18.98	–4.7860	3.4	1.7	0.199(0.020)	10.0	Blended with C_2H_5CN
151 085.05 [(*)]	$6_{1,6}-5_{0,5}$	21.24	–4.5207	4.1	1.6	0.261(0.023)	11.2	Slightly blended with C_2H_5CHO [(b)]
154 490.28 [(*)]	$3_{2,2}-3_{1,3}$	15.20	–4.9105	4.3	1.6	0.227(0.024)	9.4	Blended with C_2H_3CN
161 794.81	$5_{2,4}-5_{1,5}$	23.63	–4.6522	3.1	6.0	0.13(0.04)	3.1	Clean transition
				a-H_2C=CHOH				
72 576.63	$6_{0,6}-5_{1,5}$	19.5	–4.6023	2.0	5.0	0.096(0.021)	4.7	Clean transition
77 015.59 [(*)]	$7_{1,6}-7_{0,7}$	29.6	–4.2548	2.2	2.4	0.101(0.015)	6.6	Slightly blended with a-$^{13}CH_3CH_2OH$ [(b)]
89 757.10 [(*)]	$2_{1,2}-1_{0,1}$	5.2	–4.6954	2.1	2.0	0.167(0.013)	12.6	Clean transition [(b)]
94 064.95	$9_{1,8}-9_{0,9}$	46.0	–4.0615	1.7	1.9	0.043(0.011)	4.0	Clean transition
106 949.48 [(*)]	$3_{1,3}-2_{0,2}$	7.9	–4.4184	2.7	1.7	0.224(0.016)	14.5	Clean transition [(b)]
139 916.89 [(*)]	$9_{0,9}-8_{1,8}$	41.5	–3.8023	2.1	1.7	0.074(0.012)	6.1	Clean transition
152 530.51	$4_{2,2}-4_{1,3}$	19.6	–4.0754	1.9	6.4	0.162(0.022)	7.5 [(d)]	Clean transition [(b)]
155 160.66	$3_{2,1}-3_{1,2}$	15.8	–4.2142	2.1	6.4	0.149(0.024)	6.3 [(d)]	Blended with CH_3CHO [(b)]
232 655.55	$4_{2,3}-3_{1,2}$	19.5	–3.7853	4.5	8.3	0.21(0.06)	3.7	Clean transition

Notes. [(a)]The S/N are calculated from the integrated intensity of the lines inferred from the LTE fits of MADCUBA-SLIM. They are not calculated from the Gaussian fits of individual lines. [(b)]These transitions have been detected at the ≥3 rms noise level in peak intensity. [(c)]The error in the integrated intensity is calculated as rms$\times\sqrt{\delta v\times\Delta v}$, with δv the velocity resolution of the spectra and Δv the FWHM of the line emission of 20 km s^{-1}. [(d)]This S/N should be taken with caution since the LTE fit carried out by MADCUBA-SLIM overpredicts the integrated intensity of the line. [(*)]Transitions that provide the identification of the species with $S/N \geq 6$ in integrated intensity.

Of all these species, only vinyl alcohol has been detected in both syn and anti forms (*s*-H_2C=CHOH and *a*-H_2C=CHOH, respectively) towards G+0.693. In Table 3 and Figs. 4 and 5, we report the clean and slightly blended transitions of the syn and anti forms of H_2C=CHOH detected towards G+0.693 with an $S/N \geq 6$ (see the transitions with asterisks). The rest of lines without asterisks are also shown in Table 3 and Figs. 4 and 5 to demonstrate that they are consistent with the identification of these species and their LTE fits.

Table 3 presents four clean transitions and three slightly blended transitions of *s*-H_2C=CHOH, and three clean transitions and one slightly blended transition of *a*-H_2C=CHOH. The $4_{2,2}\rightarrow4_{1,3}$ and $3_{2,2}\rightarrow3_{1,3}$ transitions of *s*-H_2C=CHOH are blended with lines of C_2H_5CN and C_2H_3CN of similar intensity, respectively, while the $3_{2,1}\rightarrow3_{1,2}$ transition of *a*-H_2C=CHOH is blended with CH_3CHO (see Table 3). The $4_{2,2}\rightarrow4_{1,3}$ and $3_{2,1}\rightarrow3_{1,2}$ transitions of *a*-H_2C=CHOH also present an $S/N \geq 6$. However, these ratios are overestimated and should be taken with caution since they are calculated from the LTE fit of MADCUBA-SLIM and not from the Gaussian fit of the individual lines (see Table 3). As a result, these lines are not considered for the identification of *a*-H_2C=CHOH.

We derived the physical parameters of *s*-H_2C=CHOH and *a*-H_2C=CHOH using the SLIM tool from MADCUBA

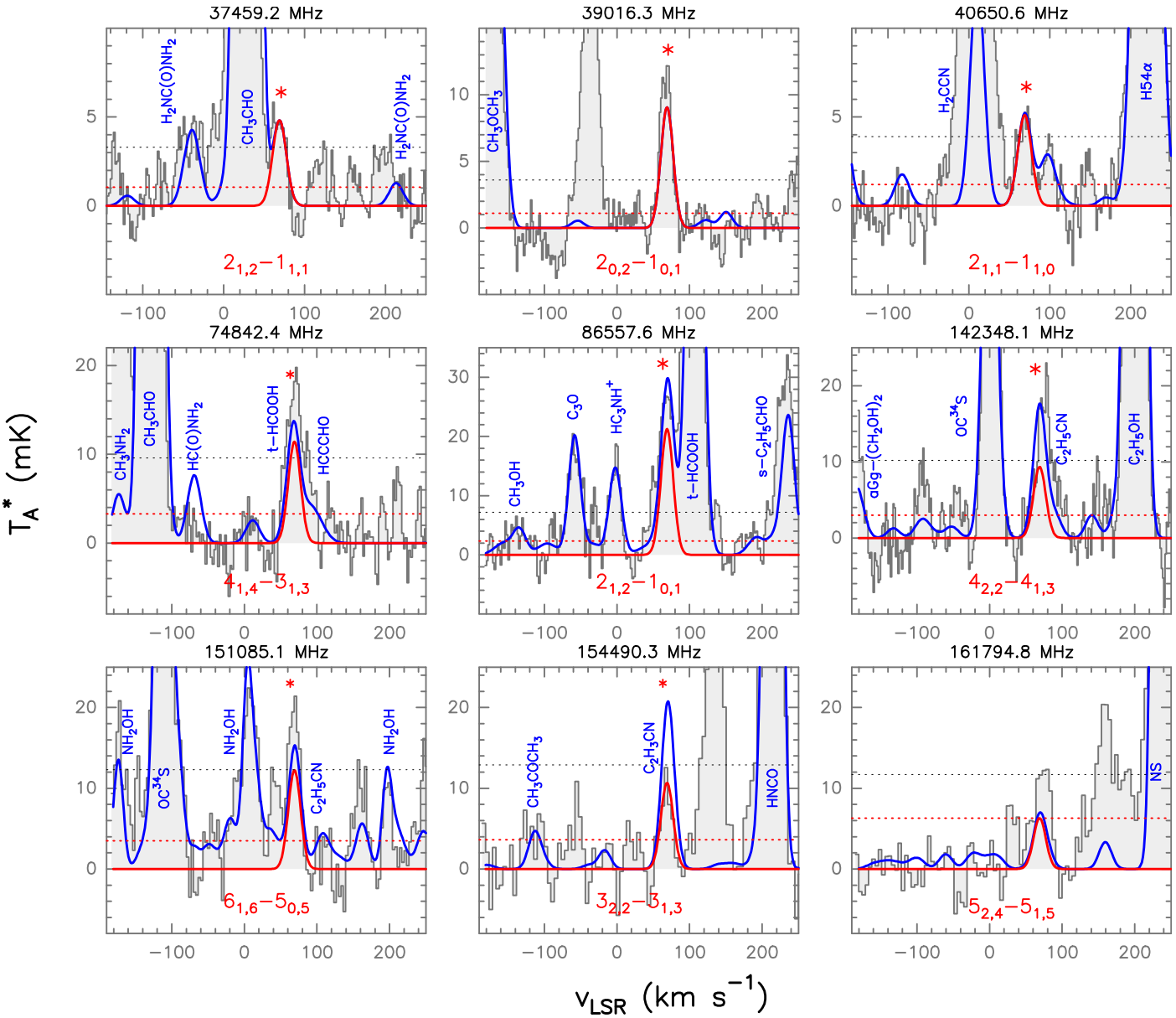

Fig. 4. Unblended and slightly blended transitions of *s*-H_2C=CHOH detected towards G+0.693. For a description of the colours displayed in the plot, see Fig. 2. The spectroscopic information and the derived parameters from the best LTE fit of these lines are reported in Table 3. The frequencies of the lines are shown in the upper part of each panel, while the red asterisks indicate the transitions that contribute to the identification of *s*-H_2C=CHOH. Dotted black lines indicate the 3 × rms level in intensity in the spectra. Dotted red lines show the detectability limit in integrated area defined as 3 × rms/ $\sqrt{N}$, with N the number of channels across the linewidth.

(Martín et al. 2019). The best LTE fit for *s*-H_2C=CHOH is obtained for a column density of $(1.11 \pm 0.08) \times 10^{14}$ cm^{-2} and an excitation temperature of $T_{ex} = 8.0 \pm 1.0$ K. For *a*-H_2C=CHOH, the best fit of the lines is obtained for a column density of $(1.3 \pm 0.4) \times 10^{13}$ cm^{-2} after fixing T_{ex} = 14 K (as we did for *Ga*-*n*-propanol), Δv = 20 km s^{-1} and V_{LSR} = 69 km s^{-1}. These results are consistent with those obtained through the rotational diagrams of *s*-H_2C=CHOH and *a*-H_2C=CHOH (see Figs. A.3 and A.4). Assuming a H_2 column density of 1.35×10^{23} cm^{-2} (Martín et al. 2008, see also Sect. 3.1), the derived column densities translate into molecular abundances of $(8.2 \pm 0.6) \times 10^{-10}$ for *s*-H_2C=CHOH, and of $(9.6 \pm 3.0) \times 10^{-11}$ for *a*-H_2C=CHOH. The syn/anti abundance ratio for H_2C=CHOH is thus ∼8.5.

By using again Equation 3 from Rivilla et al. (2019), we find a T_{kin}∼260 K, which is slightly higher than that measured towards G+0.693 (Zeng et al. 2018). If we had assumed a T_{ex} = 8.0 K (i.e. the one obtained for *s*-H_2C=CHOH), the derived column density would decrease by just a factor of 1.2, which would translate into a syn/anti abundance ratio ∼10. This ratio would be consistent with a T_{kin} ∼ 240 K, which is still higher than that determined by Zeng et al. (2018). This may mean that the two isomers of vinyl alcohol are not in thermodynamic equilibrium.

Finally, in Table 4, we report the upper limits to the column densities and abundances obtained for cyclopropanol and *n*-butanol. The upper limits to their abundance are $\leq 1.4 \times 10^{-10}$ and $\leq 4.1 \times 10^{-11}$, respectively.

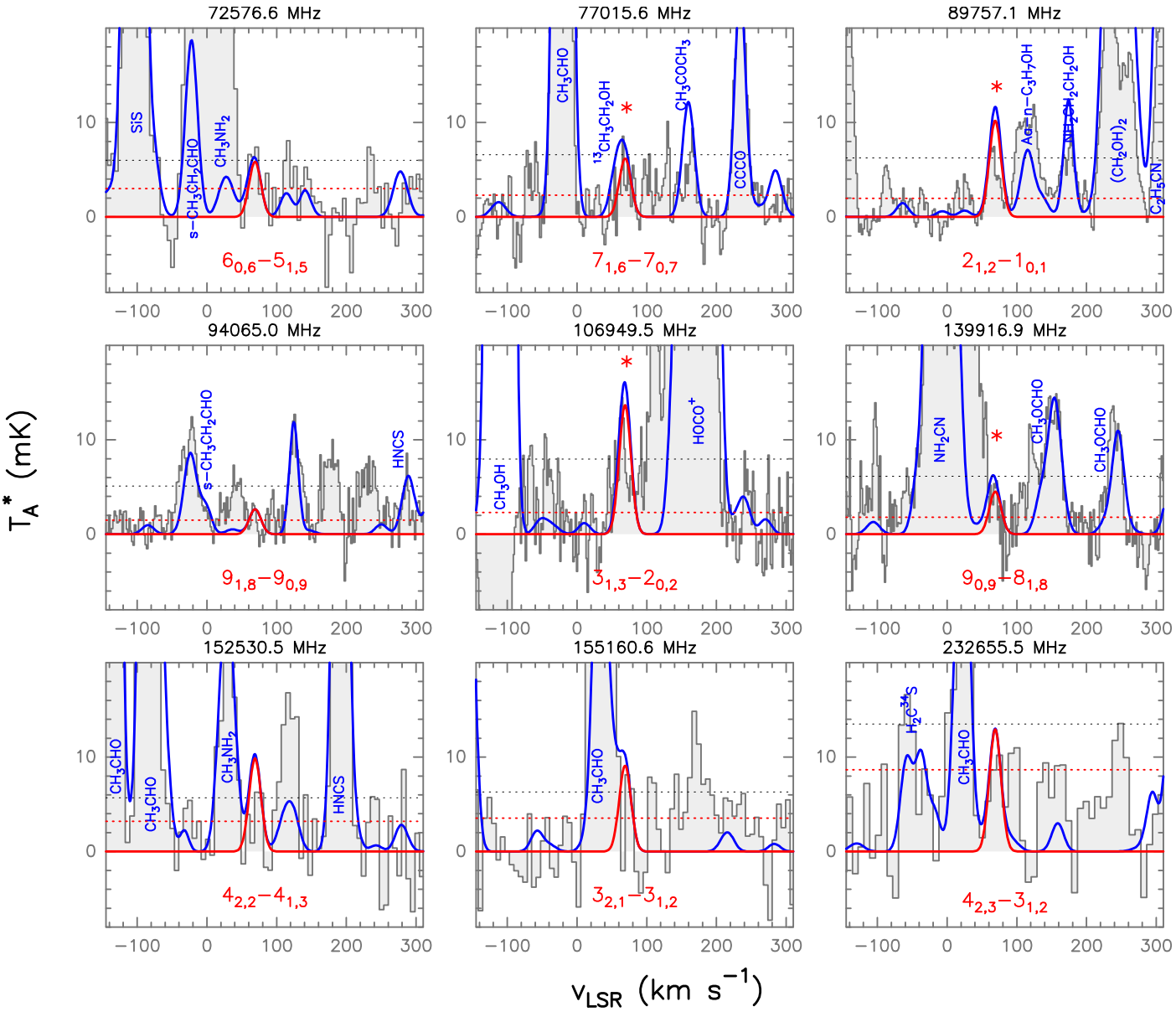

Fig. 5. Unblended and slightly blended transitions of *a*-H_2C=CHOH detected towards G+0.693. For a description of the colours displayed in the plot, see Fig. 2. The spectroscopic information and the derived parameters from the best LTE fit of these lines are reported in Table 3. The frequencies of the lines are shown in the upper part of each panel. Red asterisks indicate the transitions that contribute to the identification of *a*-H_2C=CHOH. Dotted black lines indicate the $3\times$rms level in intensity in the spectra. Dotted red lines show the detectability limit in integrated area defined as $3\times\mathrm{rms}/\sqrt{N}$, with N the number of channels across the linewidth.

Table 4. Derived upper limits to the column densities and abundances of other alcohols observed towards G+0.693.

Species	Formula	Frequency (MHz)	QNs ($J''_{K''_a,K''_c}$ - $J'_{K'_a,K'_c}$)	E_u (K)	log I(300K) (nm^2 MHz)	rms (mK)	N [a] (cm^{-2})	Abundance [b]
Cyclopropanol	c-C_3H_5OH (gauche)	93 909.6309	$3_{3,0}-2_{2,1}$	8.3	–5.5796	1.4	$\leq1.8\times10^{13}$	$\leq1.4\times10^{-10}$
n-butanol (E conf.)	*AGa*-(E)-*n*-C_4H_9OH	139 389.7073	$6_{6,1}-5_{5,0}$	22.2	–5.1710	2.2	$\leq5.5\times10^{12}$ [c]	$\leq4.1\times10^{-11}$
		139 389.7073	$6_{6,0}-5_{5,1}$	22.2	–5.1710	2.2	–	–
n-butanol (A conf.)	*AGa*-(A)-*n*-C_4H_9OH	139 389.7685	$6_{6,1}-5_{5,0}$	22.2	–5.1710	2.2	$\leq6.2\times10^{12}$ [c]	$\leq4.6\times10^{-11}$
		139 389.7685	$6_{6,0}-5_{5,1}$	22.2	–5.1710	2.2	–	–

Notes. [a]Upper limits to the column densities calculated assuming a T_{ex} = 12.5 K, i.e. the same as the one derived for *Aa*-*n*-C_3H_7OH, and after fixing V_{LSR} = 69 km s^{-1} and Δv = 20 km s^{-1} (see Sect. 3.1). [b]Abundances were derived considering a H_2 column density of 1.35×10^{23} cm^{-2} (Martín et al. 2008). [c]Upper limits were obtained considering the two transitions shown in the Table, which appear blended in the spectra.

4. Discussion

4.1. Comparison of the molecular abundances of propanol and butanol with smaller alcohols

In order to gain some insight into the production efficiency of primary alcohols in the ISM, we compared the abundances and upper limits derived for *n*-propanol (n-C_3H_7OH) and *n*-butanol (n-C_4H_9OH) with those measured for methanol (CH_3OH) and ethanol (C_2H_5OH) towards G+0.693 (see Fig. 6). The abundances of CH_3OH and C_2H_5OH towards this giant molecular cloud have been provided recently by Rodríguez-Almeida et al. (2021a) and are $(1.1 \pm 0.2) \times 10^{-7}$ for CH_3OH and $(4.6 \pm 0.6) \times 10^{-9}$ for C_2H_5OH.

From Fig. 6, it is clear that primary alcohols are produced about ten times less frequently each time a carbon atom is added to the chain (see red squares). Indeed, C_2H_5OH, n-C_3H_7OH, and n-C_4H_9OH present abundance ratios of 0.04, 0.006, and $\leq$0.0004, respectively, with respect to CH_3OH. Note that the value above and the one shown in Fig. 6 for *n*-C_3H_7OH correspond to the sum of the abundances from both *Ga* and *Aa* conformers (see Sect. 3.1). The trend of decreasing abundance by roughly one order of magnitude for increasing complexity was already noted by Rodríguez-Almeida et al. (2021a) for CH_3OH and C_2H_5OH as well as for thiols (with the -SH group). Here, we confirm that the same trend stands when the number of carbon atoms is increased to three and four within the chemical structure of primary alcohols.

By using IRAM 30 m and ALMA data, Tercero et al. (2015) and Müller et al. (2016) reported the abundances of CH_3OH and C_2H_5OH and upper limits to the abundance of *Ga*-*n*-C_3H_7OH and *i*-propanol towards Orion KL and SgrB2 (N2), respectively. The C_2H_5OH/CH_3OH abundance ratios are ~0.02 for Orion KL and ~0.05 for SgrB2 (N2), which are consistent with that found towards G+0.693 (~0.04). The upper limit to the *Ga*-*n*-C_3H_7OH/C_2H_5OH abundance ratio determined towards SgrB2 (N2) is $\leq$0.13, in agreement with the abundance ratio of ~0.14 measured towards G+0.693. For Orion KL, Tercero et al. (2015) reported a *Ga*-*n*-C_3H_7OH/C_2H_5OH abundance ratio of $\leq$0.017, that is, a factor of 10 lower than that obtained towards G+0.693. However, as noted by Müller et al. (2016), if the partition functions of C_2H_5OH and *Ga*-*n*-C_3H_7OH are corrected for conformational and vibrational contributions, this ratio becomes $\leq$0.07, which is of the same order of magnitude as those found towards SgrB2 (N2) and G+0.693.

For *i*-propanol, the upper limit to the abundance ratio with respect to CH_3OH derived towards G+0.693 is consistent with that measured in the EMoCA survey towards the SgrB2 (N2) massive star-forming region (Müller et al. 2016). While the *i*-propanol abundance upper limit in SgrB2 (N2) provides an *i*-propanol abundance that is $\geq$430 times lower than the abundance of CH_3OH, towards G+0.693 our measured upper limit gives an abundance that is $\geq$1700 times lower than that of CH_3OH (Table 2). For the remaining alcohols explored in this work, vinyl alcohol is more than two orders of magnitude less abundant than CH_3OH and a factor of 5 less abundant than C_2H_5OH, while methyl ethyl ether and cyclopropanol have abundances that are lower by factors of $\geq$500 and $\geq$800, respectively, than that of CH_3OH (see Tables 2 and 4).

Finally, if we compare the derived upper limit abundance of methyl ethyl ether ($CH_3OCH_2CH_3$) with the abundance of dimethyl ether (CH_3OCH_3) found towards G+0.693 (of 8.2×10^{-9}; Requena-Torres et al. 2006), we find that dimethyl ether is a factor $\geq$30 more abundant than methyl ethyl ether, which is also consistent with the idea that the abundance of these COMs decreases by roughly one order of magnitude with the addition of a $-CH_2$ group to their molecular structure.

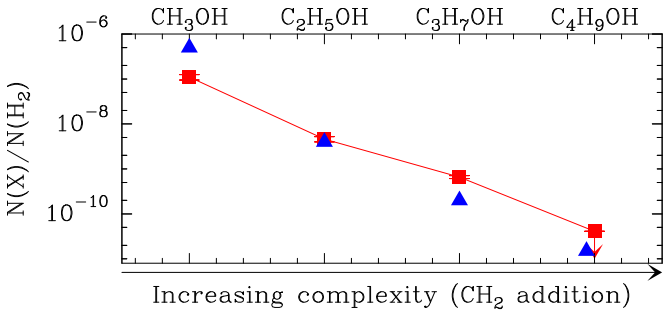

Fig. 6. Comparison of the molecular abundances of the primary alcohols methanol, ethanol, *n*-propanol, and *n*-butanol measured towards the giant molecular cloud G+0.693 (red squares) with the values predicted by the models of Charnley et al. (1995, blue triangles) for the case with initial solid abundances of 10^{-6}, 10^{-7} , and 10^{-8} for C_2H_5OH, propanol, and butanol, respectively. Error bars are also shown in red for the measured abundances, and the downward red arrow indicates an upper limit.

4.2. Chemistry of propanol and butanol in G+0.693

The chemistry of large alcohols was theoretically studied by Charnley et al. (1995) for the case of a massive hot molecular core. In this work, species such as CH_3OH, C_2H_5OH, propanol (both n-C_3H_7OH and *i*-C_3H_7OH), and butanol (n-C_4H_9OH and t-C_4H_9OH) were assumed to be formed on the surface of dust grains and injected into the gas phase by the thermal evaporation of the grain mantles. The subsequent gas-phase chemistry yields pure ethers mainly through alkyl transfer and proton transfer reactions. Charnley et al. (1995) considered that the initial ice mantle abundance of propanol and butanol were factors of 10 and 100 lower, respectively, than that of solid ethanol.

In Sect. 4.1 we reported a similar trend for these large alcohols to decrease their abundance in G+0.693 by approximately a factor of 10 with the addition of a carbon atom. If we thus compare the modelling results of Charnley et al. (1995) with our measured abundances, the best match is found for the case with initial ice mantle abundances of 10^{-6}, 10^{-7} , and 10^{-8} for C_2H_5OH, propanol and butanol, respectively. On timescales of 10^5 yr (the typical timescales that explain the rich chemistry in complex organics towards Galactic centre giant molecular clouds; see Requena-Torres et al. 2006), the predicted abundance of C_2H_5OH, propanol, and butanol in the gas phase are $\sim 4 \times 10^{-9}$, $\sim 2 \times 10^{-10}$, and $\sim 1.5 \times 10^{-11}$, respectively (see Fig. 3 in Charnley et al. 1995). These values are strikingly similar to those measured in G+0.693, that is, $(4.6 \pm 0.6) \times 10^{-9}$ for C_2H_5OH (Rodríguez-Almeida et al. 2021a), $(6.6 \pm 0.5) \times 10^{-10}$ for propanol, and $\leq 4 \times 10^{-11}$ for butanol (see blue triangles in Fig. 6). This suggests that even after gas-phase chemistry takes over, the decrease in the abundance of CH_3OH, C_2H_5OH, propanol, and butanol by roughly one order of magnitude with an increasing number of carbon atoms is preserved in the gas phase, which may allow us to indirectly constrain the amount formed in the ices for these alcohols.

We note, however, that while the modelled propanol-to-C_2H_5OH abundance ratio is 0.05 (see Fig. 3 in Charnley et al. 1995), the same ratio measured in G+0.693 gives 0.15, which suggests that propanol is more efficiently produced under the highly energetic processing of the ISM in the Galactic centre

than in typical Galactic hot cores (see Sect. 4.1 above). In addition, as pointed out by Requena-Torres et al. (2006), the models of Charnley et al. (1995) cannot explain the homogeneity of the COMs abundances across the different GMCs in the central molecular zone (or CMZ). Instead, a continuous replenishment of complex organic material from dust grains into the gas phase by large-scale shocks in the highly turbulent ISM of the Galactic centre needs to be invoked.

Charnley et al. (1995) assumed that propanol and butanol are present in ices, but did not explain how these species are formed. In the more recent chemical models of Manigand et al. (2021), propanol is formed on the surface of dust grains via two routes: (1) the successive hydrogenation of C_3O, and (2) the radical-radical reaction between O and C_3H_8. The latter has two possible outcomes, O + C_3H_8→C_3H_7OH and O + C_3H_8→H_2O + C_3H_6, with branching ratios of 20 and 80%, respectively. The models were applied to the case of the IRAS16293-2422 B low-mass hot corino, for which upper limits to the abundance of propanol were derived (Qasim et al. 2019a; Manigand et al. 2021). The results of Manigand et al. (2021) only reproduce the difference of a factor of 10 between the abundances of propanol and C_2H_5OH in the gas phase at the end of the simulations for models A1-E1, where an efficient destruction of C_3 through the gas-phase reaction O + C_3→C_2 + CO is considered (see Table D1 in this work). We note, however, that the absolute abundances of propanol and C_2H_5OH predicted by these models clearly exceed the values observed towards G+0.693 (of $\geq 10^{-7}$–10^{-6}; Manigand et al. 2021).

Laboratory experiments carried out by Qasim et al. (2019a) explored alternative formation routes for the formation of propanol in the ices such as the in situ recombination of HCO (formed after the hydrogenation of CO) with radicals formed via the processing of C_2H_2. This yields *n*-propanol after several hydrogenation steps where propenal (CH_2CHCHO) and propanal (CH_3CH_2CHO) are intermediate steps. These species have been detected towards G+0.693 with abundances of 2.7×10^{-10} for CH_2CHCHO and of 1.2×10^{-9} for CH_3CH_2CHO (see Table 4 in Requena-Torres et al. 2008)[3]. The abundance of CH_3CH_2CHO is a factor of ∼2 higher than that of *n*-propanol, which is consistent with the idea that all these species form concurrently on the surface of dust grains. Qasim et al. (2019b) also proposed that *n*-propanol and isopropanol could form in ices even at low temperatures through the radical-addition reaction between propyne (CH_3CCH) and OH. This second mechanism, however, predicts an *n*-propanol-to-isopropanol abundance ratio of 1:1, which clearly differs from that measured towards G+0.693 (abundance ratio of 1:∼0.1; see Sects. 3.1 and 3.2). The non-diffusive mechanism proposed by Qasim et al. (2019a) likely dominates the formation of these species towards G+0.693 since the dust grain temperatures in this source lie below 25 K (Rodríguez-Fernández et al. 2000).

4.3. Vinyl alcohol: comparison with previous observations

Vinyl alcohol has been reported tentatively towards the massive hot molecular core SgrB2(N) (Turner & Aponi 2001). More recently and based on a high-sensitivity spectroscopic survey carried out towards the molecular dark cloud TMC-1 with the Yebes 40m telescope, the syn conformer of vinyl alcohol (s-H_2C=CHOH) was unambiguously identified (Agúndez et al. 2021). Our observations towards G+0.693 not only confirm the presence of s-H_2C=CHOH in the ISM, but also present the first robust detection of the anti conformer of vinyl alcohol (*a*-H_2C=CHOH) in space (see Sect. 3.3).

Vinyl alcohol is a structural isomer of acetaldehyde (CH_3CHO) and therefore previous works have compared the abundance of both chemical species. Turner & Aponi (2001) showed that the column density of vinyl alcohol derived towards SgrB2(N) is similar to that measured for acetaldehyde. This is consistent with the results of Agúndez et al. (2021) towards TMC-1, where the abundance ratio s-H_2C=CHOH/CH_3CHO is ∼1. In contrast, Martin-Drumel et al. (2019) did not detect vinyl alcohol in the EMoCA survey towards the high-mass star-forming region SgrB2(N2) (Belloche et al. 2016), with an abundance ratio s-H_2C = CHOH/$CH_3CHO \leq 0.08$.

Towards G+0.693, the measured abundance of CH_3CHO is 3.7×10^{-9} (Sanz-Novo et al. 2022), while the total abundance of vinyl alcohol (considering both the syn and anti forms) is $\sim 9 \times 10^{-10}$. This implies that vinyl alcohol is less abundant by a factor of ∼4 than CH_3CHO towards the G+0.693 Galactic centre molecular cloud, with a H_2C=CHOH-to-CH_3CHO abundance ratio of 0.25 ± 0.02. This value lies between the abundance ratios found towards TMC-1 (of 1.0 ± 0.2; Agúndez et al. 2021) and SgrB2(N) (∼1, although this value has large uncertainties; see Turner & Aponi 2001), and the ratio measured towards SgrB2(N2) (≤0.08; Martin-Drumel et al. 2019). The lack of detection of vinyl alcohol towards the SgrB2(N2) compact hot cores is consistent with the idea that the emission of vinyl alcohol arises mainly from the envelope of the SgrB2 molecular cloud. In Sect. 4.4 we discuss the possible chemical routes for the formation of vinyl alcohol.

4.4. Chemistry of vinyl alcohol in G+0.693

For vinyl alcohol, both gas-phase and grain-surface formation reactions have been proposed. For gas-phase formation, Agúndez et al. (2021) concluded that the most likely mechanism for the formation of this species is the dissociative recombination of CH_3CHOH^+, for which the CCO backbone is formed with a branching ratio of 23% (Hamberg et al. 2010). The subsequent hydrogenation of CCO could form vinyl alcohol together with acetaldehyde (Agúndez et al. 2021), although the branching ratios are unknown. We also note that the gas-phase reactions OH + C_2H_4 and OH + CH_2CHCH_3 could also yield vinyl alcohol, although they present activation barriers (Zhu et al. 2005; Zádor et al. 2009).

For grain-surface reactions, vinyl alcohol has been generated in interstellar ice analogues under proton irradiation of H_2O/C_2H_2 ices (Hudson & Moore 2003) or electron irradiation of CO/CH_4 and H_2O/CH_4 ices (Abplanalp et al. 2015; Bergantini et al. 2017). More recent experiments of non-energetic processing of ices also show that the co-deposition of C_2H_2 together with O_2 and H atoms induces the formation of vinyl alcohol and acetaldehyde under low-temperature conditions (T = 10 K; see Chuang et al. 2020). Unfortunately, these works do not provide information about the branching ratios for the two species, and therefore it is not possible to assess which mechanism dominates the production of vinyl alcohol.

For the case of the Galactic centre molecular cloud G+0.693, multiple routes (both gas-phase and grain-surface) may indeed be at play since its chemistry is dominated by shocks and high cosmic-ray ionisation rates (see e.g. Zeng et al. 2018). The kinetic temperatures of the molecular gas towards this source

[3] The abundances shown in Table 4 of Requena-Torres et al. (2008) were obtained assuming a H_2 column density of 4.1×10^{22} cm^{-2}. Therefore, these abundances were corrected for the H_2 column density assumed in this work of 1.35×10^{23} cm^{-2} inferred from $C^{18}O$ data by Martín et al. (2008).

(of 70–150 K; Zeng et al. 2018) could help overcome the activation barriers of the reactions OH + C_2H_4 and OH + CH_2CHCH_3 (see above; Zhu et al. 2005; Zádor et al. 2009). In addition, although the temperature of dust is low towards this cloud, the high-radiation field of secondary UV photons (induced by the high comic-rays ionisation rate measured in the Galactic centre, which is higher by factors 100–1000 than the standard value; see Goto et al. 2014) could process the ices, generating enough radicals that could react in situ on the surface, forming vinyl alcohol. A detailed chemical modelling of the G+0.693 source is needed to asses all these different formation mechanisms. We finally note that the isomerisation transformation of acetaldehyde into vinyl alcohol is not possible (either in the gas phase or in water ices) due to the high relative energies between the two species and to the high activation energy barriers involved in this transformation (see Perrero et al. 2022).

4.5. Alcohols as precursors of lipids in primitive Earth

Understanding the emergence of membranes is central to the problem of the origin of life. Membranes are indeed a key element since they enable the encapsulation and protection of the genetic information required for replication and of nutrients needed for metabolic processes (Ruiz-Mirazo et al. 2014). Current cell membranes are formed by a bilayer of phospholipids, that is, amphiphilic molecules that contain a polar head and a non-polar hydrophobic tail. Phospholipids, however, present a rather complex structure with an alcohol phosphate group (the polar hydrophilic head, where ethanolamine is one of the possible head groups; Rivilla et al. 2021a), a glycerol, and two hydrocarbon chains derived from fatty acids (the non-polar hydrophobic tails). Because of this complexity, it is thought that these structures likely appeared biosynthetically at a later stage as a result of the machinery of the individual cell (see Ruiz-Mirazo et al. 2014, and references therein).

Alternatively, simpler amphiphilic molecules have been proposed as prebiotic lipids such as fatty alcohols or even prenols, that is single-chain unsaturated alcohols that present double bonds (Ourisson et al. 1995). These amphiphilic compounds can assemble bi-layered supramolecular aggregates such as vesicles when they come in contact with water through the so-called hydrophobic effect[4] and van der Waals interactions. The discovery in the ISM of *n*-propanol (a small chain primary alcohol) and of vinyl alcohol (a small alcohol with a double bond; see Sects. 3.1 and 3.3) thus opens the possibility that these molecules were sourced into a primitive Earth through the impact of meteorites and comets, possibly representing precursors of prebiotic lipids such as fatty alcohols and prenols. The fact that alcohols up to pentanol have not only been detected in comets such as 67P/Churyumov-Gerasimenko (Altwegg et al. 2019), but also in carbonaceous chondrites such as the Murray and Orgueil meteorites (Jungclaus et al. 1976; Sephton 2002), supports the hypothesis of an exogenous delivery of precursors of prebiotic lipids into an early Earth.

5. Conclusions

We reported the discovery of *n*-propanol in the ISM with the detection of the two lowest-energy conformers, *Ga*-*n*-C_3H_7OH and *Aa*-*n*-C_3H_7OH. *n*-propanol was detected towards the Galactic centre GMC G+0.693, which is known to be one of the richest repository of complex organic molecules in our Galaxy. The derived abundance of *n*-propanol (considering both *Ga* and *Aa* conformers) is 6.6×10^{-10}. By comparing this abundance with those of methanol and ethanol measured towards the same source, we find that the abundance of primary alcohols drops by approximately a factor of 10 by increasing complexity (i.e. by inserting a new CH_2 group).

Finally, we also reported the detection of both syn and anti conformers of vinyl alcohol (H_2C=CHOH) towards G+0.693. To our knowledge, this is the first time the latter conformer (anti) is firmly detected in the ISM. The derived abundance ratio between vinyl alcohol and acetaldehyde (its structural isomer) towards G+0.693 (of ~0.25), lies between those found toward TMC-1 and the SgrB2(N) molecular envelope (Turner & Aponi 2001; Agúndez et al. 2021), and the upper limit measured towards the SgrB2(N2) compact hot core (Martin-Drumel et al. 2019). The detection of these alcohols towards G+0.693 opens the possibility for precursors of prebiotic lipids to form in the ISM.

Acknowledgements. We would like to thank Carlos Briones for the fruitful discussions on possible prebiotic precursors of phospholipids and the formation of the first cell membranes. We also acknowledge the constructive and detailed report from an anonymous referee, who helped to improve the original version of the manuscript. Based on observations carried out with the IRAM 30m and Yebes 40m telescopes through projects 172-18 (PI: J. Martín-Pintado), 018-19 (PI: V. M. Rivilla) and 20A008 (PI: I. Jiménez-Serra). IRAM is supported by INSU/CNRS (France), MPG (Germany) and IGN (Spain). The 40 m radiotelescope at Yebes Observatory is operated by the Spanish Geographic Institute (IGN, Ministerio de Transportes, Movilidad y Agenda Urbana). I.J.-S. and J.M.-P. have received partial support from the Spanish State Research Agency (AEI) through project numbers PID2019-105552RB-C41 and MDM-2017-0737 Unidad de Excelencia "María de Maeztu" – Centro de Astrobiología (CSIC/INTA). L.F.R.-A. acknowledges support from a JAE-intro ICU studentship funded by the Spanish National Research Council (CSIC). L.F.R.-A., V.M.R. and L.C. also acknowledge support from the Comunidad de Madrid through the Atracción de Talento Investigador Modalidad 1 (Doctores con experiencia) Grant (COOL: Cosmic Origins Of Life; 2019-T1/TIC15379; PI: V.M.Rivilla). P.d.V. and B.T. thank the support from the European Research Council through Synergy Grant ERC-2013-SyG, G.A. 610256 (NANOCOSMOS) and from the Spanish Ministerio de Ciencia e Innovación (MICIU) through project PID2019-107115GB-C21. B.T. also acknowledges the Spanish MICIU for funding support from grant PID2019-106235GB-I00.

References

Abplanalp, M. J., Borsuk, A., Jones, B. M., & Kaiser, R. I. 2015, ApJ, 814, 45
Agúndez, M., Marcelino, N., Tercero, B., et al. 2021, A&A, 649, L4
Altwegg, K., Balsiger, H., & Fuselier, S. A. 2019, ARA&A, 57, 113
Bakri, B., Demaison, J., Margulés, L., & Møllendal, H. 2001, J. Mol. Spectr., 208, 92
Bar-On, Y. M., Phillips, R., & Milo, R. 2018, PNAS, 115, 6506
Becker, S., Feldmann, J., Wiedemann, S., et al. 2019, Science, 366, 76B
Belloche, A., Müller, H. S. P., Garrod, R. T., & Menten, K. M. 2016, A&A, 587, A91
Belloche, A., Garrod, R. T., Müller, H. S. P., et al. 2019, A&A, 628, A10
Bergantini, A., Maksyutenko, P., & Kaiser, R. I. 2017, ApJ, 841, 96
Bernstein, M. P., Sandford, S. A., Allamandola, L. J., et al. 1999, Science, 283, 1135
Blom, C. E., & Bauder A. 1981, Chem. Phys. Lett., 82, 492.
Charnley, S. B., Kress, M. E., Tielens, A. G. G. M., & Millar, T. J. 1995, ApJ, 448, 232
Chuang, K.-J., Fedoseev, G., Qasim, D., et al. 2020, A&A, 635, A199
Chyba, C., & Sagan, C. 1992, Nature, 355, 125
Davis, R. W., & Gerry, M. C. L. 1976, J. Mol. Spectr., 59, 407
Deamer, D. W. 1985, Nature, 317, 792
Deamer, D. W., Mahon, E. H., & Bosco, G. 1994, In Early Life on Earth, Nobel Symposium, ed. Bengtson, S. (New York: Columbia University Press), 84
Dreizler, H., & Scappini, F. 1981, Z. Nat. A., 36, 1187
Endres C. P., Schlemmer S., Schilke P., et al. 2016, J. Mol. Spectr., 327, 95
Fuchs, U., Winnewisser, G., Groner, P., De Lucia, Frank C., & Herbst, E. 2003, ApJS, 144, 277
Garay, G., & Lizano, S. 1999, PASP, 111, 1049

[4] The hydrophobic effect is the observed trend for non-polar substances to aggregate and exclude water molecules in an aqueous solution.

García de la Concepción, J., Jiménez-Serra, I., Carlos Corchado, J., Rivilla, V. M., & Martín-Pintado, J. 2021, ApJ, 912, L6
García de la Concepción, J., Colzi, L., Jiménez-Serra, I., et al. 2022, A&A, 658, A150
Goto, M., Geballe, T. R., Indriolo, Nick., et al. 2014, ApJ, 786, 96
Hamberg, M., Zhaunerchyk, V., Vigren, E., et al. 2010, A&A, 522, A90
Hudson, R. L., & Moore, M. H. 2003, ApJ, 586, L107
Ilyushin, V. V., Endres, C. P., Lewen, F., Schlemmer, S., & Drouin, B. J. 2013, J. Mol. Spectr., 290, 31
Jaman, A. I., Chakraborty, S., & Chakraborty, R. 2015, J. Mol. Struc., 1079, 402
Jiménez-Serra, I., Caselli, P., Martín-Pintado, J., & Hartquist, T. W. 2008, A&A, 482, 549
Jiménez-Serra, I., Martín-Pintado, J., Rivilla, V. M., et al. 2020, Astro. Biol., 20, 1048
Jørgensen, J. K., Belloche, A., & Garrod, R. T. 2020, ARA&A, 58, 727
Jungclaus, G. A., Yuen, G. U., Moore, C. B., & Lawless, J. G. 1976, Meteoritics, 11, 231
Kawashima, Y., Tanaka, Y., Uzuyama, T., & Hirota, E. 2021, J. Phys. Chem. A, 125, 1166
Kisiel, Z., Dorosh, O., Maeda, A., et al. 2010, Phys. Chem. Chem. Phys., 12, 8329
Macdonald, J. N., Norbury, D., & Sheridan, J. 1978, J. Chem. Soc., Faraday Trans. 2, 74, 1365
Maeda, A., Medvedev, I. R., De Lucia, F. C., & Herbst, E. 2006, ApJS, 166, 650
Manigand, S, Coutens, A., Loison, J. -C., et al. 2021, A&A, 645, A53
Margulès, L., Ilyushin, V. V., McGuire, B. A., et al. 2020, J. Mol. Spectr., 371, 111304
Marstokk, K. M., & Møllendal, H. 1973, J. Mol. Struct., 15, 137
Martín, S., Mangum, J. G., Harada, N., et al. 2021, A&A, 656, A46
Martín, S., Requena-Torres M. A., Martín-Pintado, J., et al. 2008, ApJ, 678, 245
Martín, S., Martín-Pintado, J., Blanco-Sánchez, C., et al. 2019, A&A, 631, A159
Martin-Drumel, M.-A., Lee, K. L. K., Belloche, A., et al. 2019, A&A, 623, A167
McCollom, T. M., Ritter, G., & Simoneit, B. R. T. 1999, Origins Life Evol. Biosph., 29, 153
Melosso, M., McGuire, B. A., Tamassia, F., Degli Esposti, C., & Dore, L. 2019, ACS Earth Space Chem., 3, 1189
Müller, H. S. P., Belloche, A., Xu, L.-H., et al. 2016, A&A, 587, A92
Nooner, D. W., Gibert, J. M., Gelpi, E., & Oró, J. 1976, Geochim. Cosmochim. Acta, 40, 915
Ourisson, G., & Nakatani, 1995, Y. Chem. Biol., 2, 631
Perrero, J., Enrique-Romero, J., Martínez Bachs, B., et al. 2022, ACS Earth Space Chem., 6, 496
Pszczółkowski, L. Białkowska-Jaworska, E., & Kisiel Z. 2005, J. Mol. Spectr., 234, 106
Qasim, D., Fedoseev, G., Chuang, K.-J., et al. 2019a, A&A, 627, A1
Qasim, D., Fedoseev, G., Lamberts, T., et al. 2019b, ACS Earth Space Chem., 3, 986
Requena-Torres M. A., Martín-Pintado J., Rodríguez-Fernández N. J., et al. 2006, A&A, 455, 971
Requena-Torres M. A., Martín-Pintado J., Martín S., et al. 2008, ApJ, 672, 352
Rivilla, V. M., Martín-Pintado, J., Jiménez-Serra, I., et al. 2019, MNRAS, 483, L114
Rivilla, V. M., Martín-Pintado, J., Jiménez-Serra, I., et al. 2020, ApJ, 899, L28
Rivilla, V. M., Jiménez-Serra, I., Martín-Pintado, J., et al. 2021a, PNAS, 11801314R
Rivilla, V. M., Jiménez-Serra, I., García de la Concepción, J., et al. 2021b, MNRAS, 506L, 79R
Rivilla, V. M., García de la Concepción, J., Jiménez-Serra, I., et al. 2022, Frontiers in Astronomy and Space Sciences, 9, 829288
Rodler, 1985, J. Mol. Spectr., 114, 23
Rodríguez-Almeida, L., Jiménez-Serra, I., Rivilla, V. M., et al. 2021a, ApJ, 912, L11
Rodríguez-Almeida, L., Rivilla, V. M., Jimenez-Serra, I., et al. 2021b, A&A, 654, L1
Rodríguez-Fernández, N. J., Martín-Pintado, J., de Vicente, P., et al. 2000, A&A, 356, 695
Ruiz-Mirazo, K., Briones, C., & de la Escosura, A. 2014, Chem. Rev., 114, 285
Sanz-Novo, M., Belloche, A., Rivilla, V. M., et al. 2022, A&A, in press, https://doi.org/10.1051/0004-6361/202142848
Sephton, M. A. 2002, Nat. Prod. Rep., 19, 292
Tercero, B., Cernicharo, J., López, A., et al. 2015, A&A, 582, L1
Tercero, F., López-Pérez, J. A., Gallego, J. D., et al. 2021, A&A, 645, A37
Turner, B. E., & Apponi, A. J. 2001, ApJ, 561, L207
Zádor, J., Jasper, A. W., & Miller, J. A. 2009, Phys. Chem. Chem. Phys., 11, 11040
Zeng, S., Jiménez-Serra, I., Rivilla, V. M., et al. 2018, MNRAS, 478, 2962
Zeng, S., Zhang, Q., Jiménez-Serra, I., et al. 2020, MNRAS, 497, 4896
Zhu, R. S., Park, J., & Lin, M. C. 2005, Chem. Phys. Lett., 408, 25

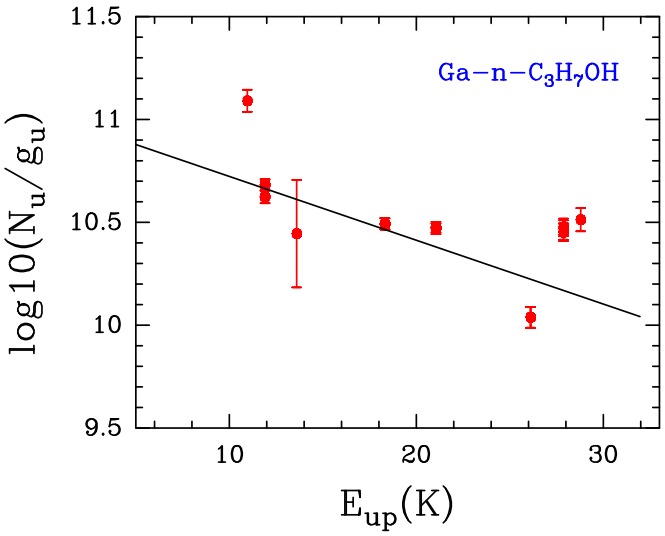

Fig. A.1. Rotational diagram obtained by using the rotational transitions of *Ga-n*-C_3H_7OH reported in Table 1. The derived parameters are T_{ex}=16.9±3.1 K and N=6.6±2.3×10^{13} cm^{-2}.

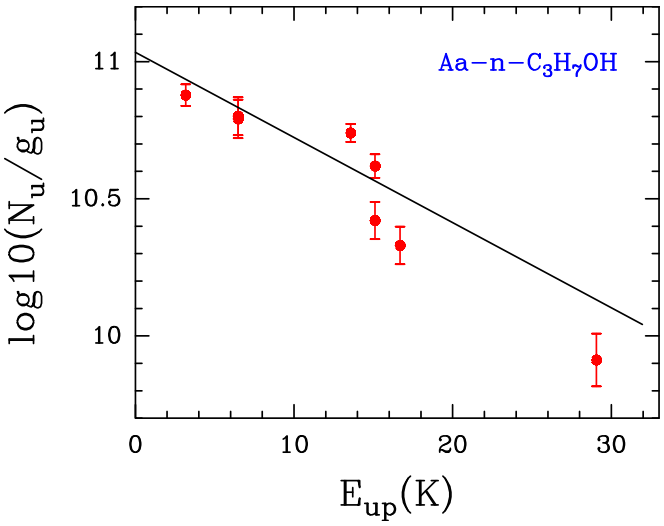

Fig. A.2. Rotational diagram obtained by using the rotational transitions of *Aa-n*-C_3H_7OH reported in Table 1, except the $9_{2,8}$→$9_{1,9}$ and $10_{1,10}$→$9_{0,9}$ lines that are blended with U species. The derived parameters are T_{ex}=14.0±3.4 K and N=5.1±2.2×10^{13} cm^{-2}.

Appendix A: Rotational diagrams

In this section, we show the rotational diagrams obtained for *Ga-n*-C_3H_7OH, *Aa-n*-C_3H_7OH, *s*-H_2C=CHOH, and *a*-H_2C=CHOH (see Figures A.1, A.2, A.3, and A.4), which have been detected towards G+0.693. The goal is to establish the reliability of the excitation temperatures (T_{ex}) and column densities (N) derived by MADCUBA (see Sections 3.1 and 3.3). For these diagrams, we used all molecular transitions reported in Tables 1 and 3, except for *Aa-n*-C_3H_7OH, for which we did not consider the $9_{2,8}$→$9_{1,9}$ and $10_{1,10}$→$9_{0,9}$ transitions, which appear blended with U species.

The results of the rotational diagrams are T_{ex}=16.9±3.1 K and N=6.6±2.3×10^{13} cm^{-2} for *Ga-n*-C_3H_7OH, T_{ex}=14.0±3.4 K and N=5.1±2.2×10^{13} cm^{-2} for *Aa-n*-C_3H_7OH, T_{ex}=8.715±0.008 K and N=1.5±0.3×10^{14} cm^{-2} for *s*-H_2C=CHOH, and T_{ex}=17.0±2.4 K and N=1.5±0.4×10^{13} cm^{-2} for *a*-H_2C=CHOH. These values are consistent with those obtained by MADCUBA.

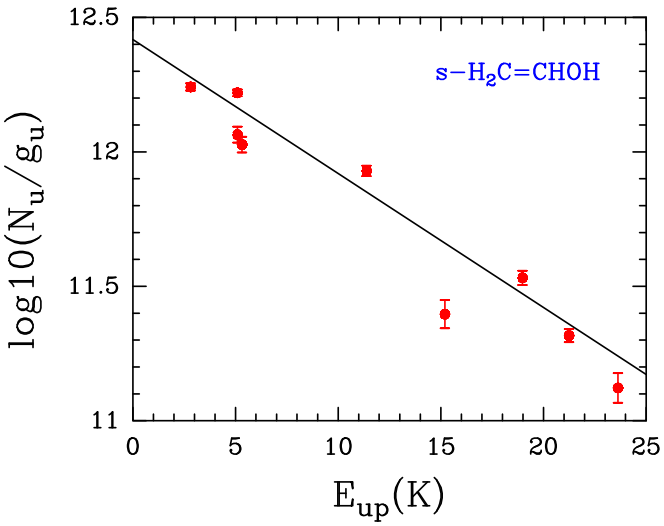

Fig. A.3. Rotational diagram obtained by using the rotational transitions of *s*-H_2C=CHOH reported in Table 3. The derived parameters are T_{ex}=8.715±0.008 K and N=1.5±0.3×10^{14} cm^{-2}.

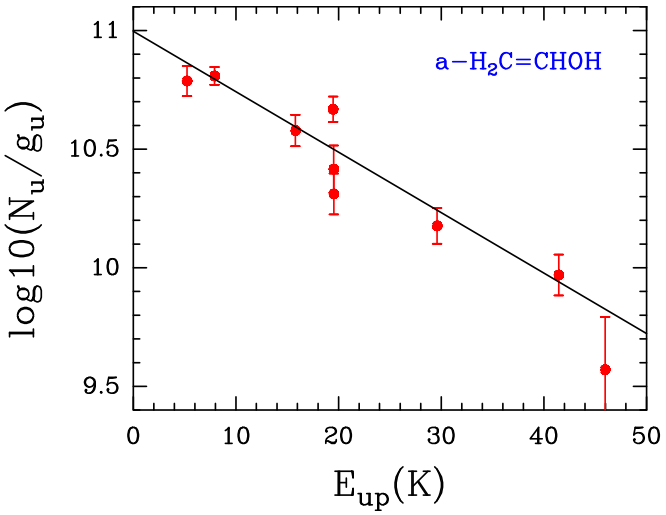

Fig. A.4. Rotational diagram obtained by using the rotational transitions of *a*-H_2C=CHOH reported in Table 3. The derived parameters are T_{ex}=17.0±2.4 K and N=1.5±0.4×10^{13} cm^{-2}.